ICARUS **126,** 28–41 (1997)
ARTICLE NO. IS965634

Evolution of the G Ring and the Population of Macroscopic Ring Particles

ROBIN M. CANUP AND LARRY W. ESPOSITO

Laboratory for Atmospheric and Space Physics, University of Colorado, Box 392, Boulder, Colorado 80309–0392
E-mail: canup@sargon.colorado.edu

Received June 19, 1996; revised September 30, 1996

An evolutionary model of the G Ring incorporating theoretical results from R. M. Canup and L. W. Esposito (1995, *Icarus* 113, 331–352) yields a complete particle size distribution that is consistent with existing observations. Results from numerical modeling demonstrate that a G Ring origin from the disruption of a 1.5-3 km progenitor satellite can match all known properties of the ring. In addition, we estimate the population of unseen macroscopic material from both observational upper limits and our theoretical model for the region surrounding the G Ring, where the Cassini spacecraft will likely make its innermost passes in the saturnian system. For models that fit all available data, the probability of Cassini striking a hazardous ring particle is less than 1%.

I. BACKGROUND

The G Ring of Saturn, first observed by Voyager 1, is a narrow and tenuous dust ring located between 2.75 and $2.88R_S$ with a mean optical depth of about 10^{-6}. A recent reanalysis of Voyager photometric images of the G Ring by Showalter and Cuzzi (1993) reveals a ring whose optical depth is dominated by extremely small, short-lived dust particles ($r \geq 0.03$ μm) described by a steep power-law size distribution. Charged particle absorption data from Pioneer 11 constrains the total surface area of large bodies in the ring to 10–40 km^2 (e.g., Van Allen 1983) within a region about 1000 km in width.

Interest in the G Ring has recently grown due to both the first Earth-based observations of the ring (obtained in the summer of 1995 during the Saturn ring plane crossing) and the upcoming Cassini mission to Saturn. The Cassini spacecraft will make its inner-most crossings of Saturn's equatorial plane in the region surrounding the G Ring, between the outer edge of the A Ring ($a = 2.27R_S$) and the orbit of Mimas ($a = 3.1R_S$). While the orbital tour will avoid areas where ring material has already been detected, the observational upper limits on the optical depth of material in the "empty" regions are consistent with a significant population of macroscopic particles capable of critically damaging the spacecraft (those with $r \gtrsim 0.13$ mm or $m \gtrsim 10^{-5}$ g). Previous work by Divine (1989) evaluated the vulnerability of components of the spacecraft to impact by particles at 7–15 km/sec, corresponding to relative velocities for Cassini ring plane crossings in low to highly inclined orbits. Ring particles larger than 0.13–1.0 mm in radius are capable of puncturing critical spacecraft subsystems, the most sensitive of which range in cross-sectional area from 0.05 to 3.17 m^2 (Tan and Tsuyuki 1989). Divine considered various models for the size distribution of particles in the micrometer to centimeter size range for orbital radii greater than $2.37R_S$ (exterior to the A Ring) which were consistent with the observational upper limits and charged particle absorption data from Pioneer 11. These models yield a wide range of expectation values for the number of critically injuring impacts experienced by Cassini per ring plane crossing, from 10^{-8} to 0.4 (Divine's Table 6), all consistent with the existing observations.

In this work we adopt an alternative approach. We consider an evolutionary model of the G Ring constrained to match the existing observational data. In this model, the origin of the ring is associated with the catastrophic fragmentation of a progenitor satellite by a meteoroid or cometary impact (see, e.g., Colwell and Esposito 1992, 1993, Showalter and Cuzzi 1993). The largest remaining fragments from the initial disruption become G Ring parent bodies, which act as sources for the observed dust ring. Our model tracks the ring particle population as it evolves due to (1) accretion onto parent bodies, (2) collisional release as parent bodies collide, (3) production due to ejection by meteoroid impact into the parent bodies, and (4) removal due to both plasma drag and catastrophic fragmentation. Predicted ring particle populations are consistent with Voyager photometry (Showalter and Cuzzi 1993), Voyager dust impact detections during the G Ring crossing (PWS/PRA instruments, Gurnett *et al.* 1983), and parent body surface-area constraints from Pioneer 11 charged particle absorption data (Van Allen 1983).

We predict the steady-state population of material in

0019-1035/97 $25.00

the G Ring as a function of initial conditions and process rates. Motivated by an interest in assessing the potential ring hazard to the Cassini spacecraft, we estimate the total amount of macroscopic material ($r \geq 0.13$ mm) in the G Ring. Our estimates are orders of magnitude smaller than those derived from the observational upper limits in the surrounding regions, where no particles are observed. Since the apparently empty regions are likely populated by processes similar to those in the G ring, even lower limits may be set for the population of particles hazardous to Cassini existing just outside the observed G Ring.

In Section II we calculate observational limits on the population of unseen macroscopic ring material that may exist in the G Ring region. In Section III we discuss the main physical processes in the G Ring and describe an evolutionary model of the ring in Section IV. Our simulation results are presented in Section V, including steady-state ring size distributions. In the final section, we discuss the implications of our results for the history of the G Ring and present improved estimates of the population of macroscopic ring material.

II. OBSERVATIONAL LIMITS ON UNSEEN RING MATERIAL

The G Ring is an extremely faint ring, visible in only two Voyager images with a peak brightness significantly less than brightness variations in the surrounding background (Showalter and Cuzzi 1993, hereafter SC93). Accordingly, recent photometric analysis of the Voyager images by SC93 used a subtraction technique that modeled background brightness variations assuming that the G Ring is an isolated feature surrounded by empty space. In the following sections, we discuss observational limits on the presence of a background population of macroscopic particles in the G Ring region that would have been undetected by the SC93 analysis.

Photometric Limits

The upper photometric limit for particles much larger than the wavelength of light (for the visible observations, typically $\lambda \sim 0.5$ μm) outside the G Ring is $\tau \leq 6 \times 10^{-7}$ (Divine 1989, Cuzzi *et al.* 1989). In the extreme case of a single-size particle population, the vertically integrated surface number density, σ_n, is

$$\sigma_n = \frac{\tau_0}{\pi r_0^2}, \tag{1}$$

where τ_0 is the optical depth of radius r_0 particles. For example, if the background population is composed solely of 0.13-mm-radius particles, then $\sigma_n \approx 11\ \mathrm{m}^{-2}$. Thus, photometric upper limits are consistent with an unobserved background population density of up to ~10 macroscopic particles per square meter of ring plane surface area integrated over the entire vertical extent of the ring material.

Charged Particle Absorption Data

Van Allen (1983) modeled the absorption of charged particles by an optically thin ring and demonstrated that proton lifetime is inversely related to the surface mass density of ring material if the absorbing material is smaller than the typical distance required to stop a proton (~25 cm). Hood (1989) analyzed the Pioneer 11 charged particle absorption data and estimated an upper limit on proton lifetimes just outside the G Ring of 10^9 sec (consistent with no absorption at $a = 2.67 R_S$). This lifetime implies an upper limit on the surface mass density of particles smaller than ~25 cm of $\sigma_m \leq 10^{-8}$ g/cm^2 (see Showalter and Cuzzi 1993). If σ_m were composed entirely of 0.13-mm-radius particles we would have a maximum optical depth of $\tau_0 = 5.8 \times 10^{-7}$ and a surface number density of

$$\sigma_n = 10.9\ \mathrm{m}^{-2}, \tag{2}$$

a limit close to that predicted above from photometric upper limits.

Voyager 2 PWS/PRA Particle Detections

The dust impact detections by the PWS/PRA instruments cannot be used to directly estimate the population of unseen macroscopic particles without making inferences about particle size distributions, since these detections are sensitive only to particles near 10 μm in radius. We will, however, use the PWS/PRA results as a check on our theoretically predicted dust populations, and so we discuss them now.

When Voyager 2 crossed the ring plane of Saturn near the outer edge of the G Ring at $2.86 R_S$, both the plasma wave and the planetary radio astronomy instruments detected bursts of intense noise which have been associated with the impact of dust particles on the spacecraft (e.g., Gurnett *et al.* 1983, Tsintikidis *et al.* 1994). If the detected signals were caused by impact ionization occurring as grains collided with the craft, assumptions about the charge yield during an impact and the collection coefficient of the spacecraft (the portion of the released charge collected by a given instrument's antenna) give estimates of the number density and mass of the impacting particles.

In a recent reanalysis of the ring plane impact data, Tsintikidis *et al.* (1994) estimate the root-mean-square mass of impactors with mass greater than 5.4×10^{-9} g to be $\langle m^2 \rangle^{1/2} = 1.8 \times 10^{-8}$ g (or $r = 16.4$ μm). Uncertainty in the collection coefficient and the proportionality constant between the mass of impacting particle and the total re-

leased charge leads to at least an order of magnitude uncertainty in this estimate (Tsintikidis *et al.* 1994).

Prior Successful Passages

There have been four previous safe passages through the Saturn ring plane by spacecraft at distances of 2.78, 2.88, 2.92, and $6.3 R_S$. These spacecraft were ideal detectors of macroscopic ring particles, and their prior successful crossings can also be used to provide an upper limit on any smooth background of particles in the ring plane. Such a smooth background would be very difficult to detect in the optical observations.

For ring particles randomly distributed in Saturn's equatorial plane the impact of a spacecraft with a particle can be modeled as a Poisson process, giving the probability of safe passage (e.g., Divine 1989)

$$P_0 = e^{-AF_A}, \tag{3}$$

where A is the vulnerable area of the spacecraft projected perpendicular to the flight path, and F_A is the fluence, or path-integrated flux, of dangerous particles. The fluence (in cm^{-2}) is

$$F_A \approx \frac{H}{\sin i} \int_{r_0}^{r_{max}} n(r)\, dr = \frac{\sigma_n}{\sin i}, \tag{4}$$

where H is the vertical ring height, i is the angle between the spacecraft's orbit and the ring plane, r_0 is the minimum hazardous particle size, and $n(r)\, dr$ is the volume number density of particles of radius $r \rightarrow r + dr$, where we have assumed the ring particles can be considered motionless relative to the spacecraft (a good approximation except for $i \approx 0$ crossings). For ring particles all the same size, the expected number of impacts to a spacecraft per crossing, AF_A, is

$$AF_A = \frac{A}{\pi r_0^2} \frac{\tau_0}{\sin i}, \tag{5}$$

where τ_0 is the optical depth of particles of radius r_0. For small values of AF_A, the probability of safe passage is approximately $P_0 \approx (1 - AF_A)$.

If we consider that four prior safe spacecraft passages was a very fortunate event with a probability of only 1%, then from Poisson statistics, $e^{-4AF_A} > 0.01$, or $AF_A < 1.15$. For a choice of $\sin i \approx 0.5$ and hazard threshold values typical for Voyager and Cassini this yields a surface number density with 99% confidence of

$$\sigma_n < 11.5\ m^{-2} \tag{6}$$

for particles with $r > 0.13$ mm. We note that this simple estimate of macroscopic particles derived from our past experience is comparable to the observational upper limits from photometry and charged particle absorption. This is because a spacecraft like Pioneer or Voyager provides a well-matched detector for the macroscopic regime of the ring particle distribution, while the photometry and particle data are more sensitive to smaller ring particles.

Thus, the observational upper limits in the "empty" regions of Saturn's equatorial plane are consistent with significant populations of unseen macroscopic particles. Stronger limits can come from improved knowledge of the particle size distributions; since we have not yet observed any particles in these regions, we consider the best approach to be a theoretical model of the physical processes occurring in these outer rings. In the sections that follow, we develop an evolutionary model of the G Ring consistent with observations. This model can then be used to predict the steady-state size distribution of material in the G Ring, including a direct estimate of the population of macroscopic particles. These estimates are orders of magnitude smaller than those derived from the observational upper limits in the surrounding "empty" regions.

III. G RING PROCESSES

Showalter and Cuzzi's (1993) photometric analysis of Voyager G Ring images reveals an optical depth dominated by small dust particles ($r \gtrsim 0.03\ \mu m$) fitted by an unusually steep power-law size distribution (differential size index, $q \sim 6$). The lifetimes of these dust particles against removal by drag and destructive forces range from ~1 to 1000 years for 0.03- to 1-μm radius particles (Burns *et al.* 1984). SC93 thus conclude that the G Ring contains a population of parent bodies that act as a continuing supply of ring particles similar to those proposed for Jupiter's ring (Burns *et al.* 1980) and the uranian and neptunian dust rings (Esposito and Colwell 1989, Colwell and Esposito 1990, 1992, 1993). The Pioneer 11 particle absorption data provide an upper limit on the total cross section of bodies contained in the G Ring with $r > 25$ cm (see above). It is likely that the parents are much larger than this, given that a 25-cm radius body would have a lifetime of only 10^6 years against meteoroid erosion (SC93). The estimated proton lifetime of 1.1×10^8 sec at the G Ring (Hood 1989, Van Allen 1983) implies a cross-sectional area of parent bodies of 10–40 km^2. The Pioneer absorption signatures also indicate the presence of multiple absorbing bodies, as they resemble those characteristic of narrow rings rather than that of a single moon (e.g., SC93).

SC93 suggest that the G Ring parent bodies are the remaining fragments from the disruption of a progenitor

satellite. A similar scenario has been modeled by Colwell and Esposito (1992, 1993) to account for the origin of narrow rings around Uranus and Neptune. Colwell and Esposito (1992, 1993) demonstrated that the formation of a narrow debris ring is the natural outcome of satellite fragmentation, and proposed that disruptions with impact velocities large enough to be near the catastrophic fragmentation threshold would yield moonlet belts that act as sources for dusty rings. This is a plausible origin scenario for the G Ring given that a 3-km-radius progenitor body at $2.8R_S$ would have a lifetime against catastrophic disruption of about 10^8–10^9 years using the Colwell and Esposito (1992) impactor flux model (Joshua Colwell, personal communication).

The debris produced by the initial disruption of the hypothetical G Ring progenitor satellite would have a mass distribution related to the energy of the disrupting impactor. Housen and Holsapple (1990) parameterized data from several experimenters and found that the mass fraction of the largest fragment, f_l, is a function of the impact energy,

$$f_l = 0.5\left(\frac{Q^*}{Q}\right)^{1.4}, \tag{7}$$

where Q is the specific impact energy (the kinetic energy of the impactor divided by the mass of the target) and Q^* is the specific impact energy at the catastrophic fragmentation threshold (defined so that $f_l = 0.5$ when $Q = Q^*$). Colwell and Esposito (1992) calculated probability distributions for Q (with $Q \geq Q^*$) and f_l by integrating over their impactor flux and velocity distribution and defining Q^* as a function of material constants, target radius, and impact velocity [from Housen and Holsapple 1990; see Colwell and Esposito 1992, Eq. (7)]. For a 3-km-radius target the median value is $f_l \sim 0.16$, while the most likely value is $f_l = 0.5$.

Experimental data show that the slope of the debris mass distribution is a function of f_l. In general, more energetic disruptions lead to smaller values of f_l and steeper debris size distributions. Davis and Ryan (1990) find that the differential mass power-law index for debris smaller than 1–2% of the initial target mass is approximately

$$q_m \approx 1.0 + \frac{0.2}{\sqrt{f_l}}, \tag{8}$$

with $n(m)\ dm = Cm^{-q_m}\ dm$. Since the specific kinetic energy of the proposed disruption that formed the G Ring is unknown, f_l is a free parameter in the following analysis.

The median velocity of the fragments following a satellite disruption is on the order of the escape velocity of the progenitor, or in this case 1–2 m/sec (Colwell and Esposito 1993). Collisions between the fragments would not have caused further fragmentation or substantial breakage; experimental data show collisional shattering only for $v_{imp} >$ 100 m/sec and no chipping for $v_{imp} < 10$ m/sec (i.e., Greenberg *et al.* 1978). Thus, production of additional debris due to collisions between the fragments would likely not have been significant.

Limited accretion would have occurred between fragments that differed in size. In two previous works (Canup and Esposito 1995, 1996) we developed a tidal accretion model valid for accretion near the Roche limit. Our model demonstrates that in the Roche zone ($a < 1.4a_{Roche}$, where a_{Roche} is the classical Roche limit), tidal forces prevent like-size bodies from remaining gravitationally bound, even for completely inelastic collisions. At the G Ring, small debris will accrete onto the surface of the largest fragments, but the largest bodies will be prevented from accreting with one another due to the tidal forces of the planet. This provides a natural explanation for the multiple source bodies in the G Ring. The size range over which accretion is tidally precluded is a function of the debris density, orbital radius, and mass of the largest fragment [see Canup and Esposito 1995, Eq. (35)]. For a density of 1 g/cm^3 and a coefficient of restitution of $\varepsilon = 0.25$ [Weidenschilling and co-workers' (1984) choice for irregular ice spheres], fragments with masses between about (0.08–1.0) f_l times the mass of the progenitor satellite will accrete regoliths of smaller particles but will be unable to accrete with one another. These few largest fragments would act as G Ring parent bodies both for the dust we see now and for particles potentially hazardous to the Cassini spacecraft.

For as long as the parent bodies remain in crossing orbits, a collisional balance will be established between accretion of debris onto the parent bodies and release of previously accumulated debris as parent bodies collide with one another. The steady-state fraction of debris in the unaccreted free state in this balance can be estimated analytically from the volume fraction of regolith ejected when two parent bodies collide, δ (see Canup and Esposito 1995, Section IV). The number fraction of debris in the free state is approximately

$$X_{eq} \sim \left[1 + \frac{1}{\delta}\right]^{-1}. \tag{9}$$

In Canup and Esposito (1995) we used crater scaling arguments to estimate the fraction of regolith released when two like-sized moonlets collide to be $\delta = 0.12$ (see also next section). This estimate yields $X_{eq} \sim 0.1$, or that ~90% of the small particles will reside in the regoliths of the parent bodies in a steady state between collisional release and reaccretion.

The size distribution of G Ring material is also affected

by ongoing creation and destruction processes. High-velocity external impactors (meteoroid or cometary) will erode the parent bodies and act as a source for ring particles, which will be removed by drag or destructive forces (see, e.g., SC93, their Section 6). These processes make the total number and size distribution of particles in the system time dependent and preclude an analytical steady-state solution. In the following section we describe a simple evolutionary model that includes these processes.

IV. EVOLUTIONARY MODEL

In our model, the mass distribution of G Ring debris at a given time is determined by two state vectors, N and n. N_i is defined to be the total number of bodies in the system with masses between m_i and $2m_i$; this quantity includes both particles in free orbits and those that have accreted onto the parent bodies and are contained in regolith. The number of particles in the free state with masses between m_i and $2m_i$ is just n_i.

The distribution of parent bodies depends on the energy of the initial G Ring-forming impact event, which determines both the parameters f_l, the mass fraction of the largest fragment, and q, the slope of the postdisruption fragment population. The Canup and Esposito (1995, 1996) tidal accretion model determines the mass range of fragments that remain dispersed as a belt of parent bodies; for a density of 1 g/cm^3 and a coefficient of restitution of $\varepsilon = 0.25$, fragments with masses between $0.08\,f_l$ and $1.0\,f_l$ times the mass of the progenitor satellite are too close in size to accrete upon mutual collision, and we define these as the parent bodies. For each choice of initial impact energy, the size of the progenitor satellite (and thus the total initial mass in the system) is fixed by constraining the cross-sectional area of the parent bodies to a value matching the P11 proton absorption data, 10–40 km^2.

The evolving distribution of free particles is determined by four main processes: accretion onto parent bodies, release during parent body collisions, production as ejecta from meteoroid impacts into the parent bodies, and removal by both plasma drag and catastrophic fragmentation. The size distribution of regolith on the parent bodies also evolves with time: material is added to the regoliths as parent bodies sweep up free ring particles and removed as collisions between parent bodies knock off previously accreted debris. The rates of all processes are computed at each time step and used to update the mass distribution state vectors. The time step size for the calculation is adjusted so that no mass bin loses or gains more than 10% of its particles during a single time step.

Accretion onto Parent Bodies

In the ''particle-in-a-box'' approximation, the rate of change in the number of free particles in mass bin i due to accretion onto the parent bodies is (see Canup and Esposito 1995, 1996)

$$\left.\frac{dn_i}{dt}\right|_{\rm acc} \approx -\frac{n_i \sigma_{\rm par} \Omega}{2\pi a\,\Delta a} \approx -n_i \tau_{\rm par} \Omega, \qquad (10)$$

where $\sigma_{\rm par}$ and $\tau_{\rm par}$ are the total cross-sectional area and optical depth of the parent bodies, Ω is orbital frequency, Δa is the radial width of the ring, and we have approximated the height of the ring by $v_{\rm ran}/\Omega$. Hood's (1989) reanalysis of the G Ring proton absorption signatures suggests that most of the ring's mass is contained within a narrow band ~1000 km in width. For $\sigma_{\rm par} = 40$ km^2 and $\Delta a = 1000$ km, $\tau_{\rm par} = 4 \times 10^{-8}$ and the collision time of a particle with a parent body is given by $1/\tau\Omega = 8900$ years. Equation (10) assumes that all collisions between debris particles and parent bodies result in accretion. We ignore the effect of accretion between free debris particles.

Release during Parent Body Collisions

Assuming that low-velocity collisions between parent bodies result in release of previously accumulated debris but do not yield significant erosion and creation of additional debris, the rate of change of free particles can be approximated by

$$\left.\frac{dn_i}{dt}\right|_{\rm rel} \approx \frac{2(N_i - n_i)}{N_{\rm par}}\,\delta(4\tau_{\rm par}\Omega), \qquad (11)$$

where the quantity $2(N_i - n_i)/N_{\rm par}$ is the number of particles with mass between m_i and $2m_i$ contained in the regoliths of a pair of colliding parent bodies, $N_{\rm par}$ is the total number of parent bodies, δ is the fraction of regolith released when two parent bodies collide, and $1/(4\tau\Omega)$ is the approximate time for a parent body to collide with another like-sized parent body [assuming a mutual geometric collisional cross section of $\pi(r_{\rm par} + r_{\rm par})^2$, or $4\pi r_{\rm par}^2$].

The determination of an appropriate value for δ is difficult given that there are few experimental data for ejecta production during low-velocity ($\lesssim$1–10 m/sec) collisions. Given this constraint, Canup and Esposito (1995) used a simple ejecta scaling argument to estimate the fraction of the crater volume that would escape when two like-sized moonlets collide. We assumed that ejecta release between bodies covered in loosely bound regolith is best described by the ''gravity regime'' ejecta scaling relations (ignoring any internal strength of the regolith) for impacts into sand, that no fragmentation of the solid parent body cores occurs, and that the average escape velocity is reduced from the two-body escape velocity due to tidal forces at the G Ring's orbit. This approach yielded an estimate that ~75% of the

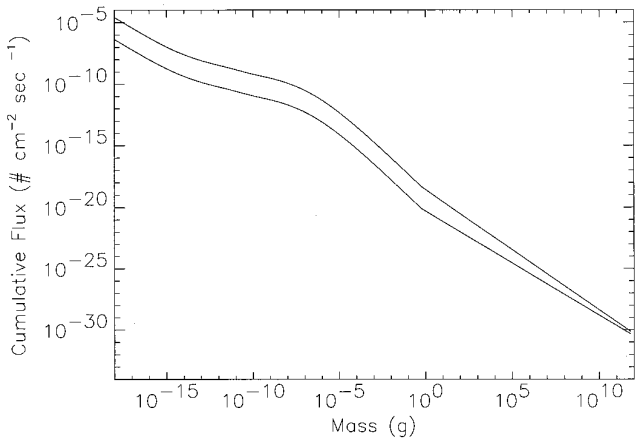

FIG. 1. Cumulative impactor fluxes are plotted as a function of impactor mass. The two models used in this work are shown by the solid lines. Both models are based on the Grün *et al.* (1985) estimates for masses up to 1 g and match the observed rate of cratering on the satellite Mimas (Smith *et al.* 1982).

crater volume would escape, or that ~12% of the total regolith on the colliding bodies would be lost during a single collision (assuming a uniform regolith depth) corresponding to $\delta = 0.12$. For lack of better scaling relations, we retain this estimate here.

Production due to Meteoroid Erosion of Parent Bodies

High-velocity meteoroid impacts into the parent bodies will cause ejection of debris and production of new ring material. For the flux of impactors we consider both a high-flux model and low-flux model, both shown in Fig. 1. The high-flux model uses the micrometeoroid flux of Grün *et al.* (1985) at 1 AU for masses up to 1 g; the low-flux model extrapolates the Grün *et al.* flux to 9.5 AU using their $r^{-1.8}$ dependence, which yields a factor of 50 decrease. The cumulative fluxes in Fig. 1 do not include gravitational focusing by Saturn. The impactor flux at radius a from Saturn will be increased from that shown in Fig. 1 by a factor f_s due to Saturn's gravity:

$$f_s = \left(1 + \frac{GM_S}{av_\infty^2}\right), \tag{12}$$

where $\sqrt{2GM_S/a}$ is the escape velocity of Saturn at a, and v_∞ is the velocity of the impactor far from Saturn (e.g., Colwell 1994). Oort cloud and planet family impactors have a mean v_∞ of about $\sqrt{2}v_{orb}$, where v_{orb} is the orbital velocity of the planet being considered (Cuzzi and Durisen 1990). For Saturn, this gives $v_\infty \approx 13.7$ km/sec, or $f_s \approx 2.2$ at the orbit of the G Ring.

To determine the flux of larger impactors, we use Smith and co-workers' (1982) estimate of the present rate of production of craters 10 km or larger on the satellite Mimas. The crater diameter scaling law appropriate for impacts into hard surfaces is $D = 4.9 \times 10^{-3} E_I^{1/3}$ cm (Housen *et al.* 1979), where E_I is the kinetic energy of the impactor. In the two-body approximation, impact velocity is a function of the escape velocity of Saturn at the orbit of Mimas (approximately 21 km/sec) and the velocity of the impactor far from Saturn: $v_{imp}^2 = v_\infty^2 + v_{esc}^2$. A mean v_∞ of 13.7 km/sec yields an impact velocity of 25 km/sec, so that an impactor of mass 2×10^{13} g would produce a 10-km crater on Mimas. The Smith *et al.* (1982) rate of production of craters larger than 10 km [$N(D > 10 \text{ km}) \sim 5.1 \times 10^{-32}$ cm^{-2} sec^{-1}] can then be translated to an impactor flux (reduced by the appropriate f_s): $N(\geq 2 \times 10^{13}\text{g}) = 2.3 \times 10^{-32}$ cm^{-2} sec^{-1}. The slope of the cumulative impactor flux for large impactors for both our high- and low-flux models is determined by matching this value to the Grün *et al.* (1985) flux at 1 g. This yields a cumulative mass power-law index of $b_m = 0.98$ in the high-flux model and $b_m = 0.85$ in the low flux model. This approach is analogous to that used by Colwell and Esposito (1990), who extrapolated the large impactor flux at Uranus from the observed cratering rate of 10-km craters on the satellite Cordelia.

The rate of production of free particles in mass bin i due to meteoroid bombardment is just

$$\left.\frac{dn_i}{dt}\right|_{ej} \approx \frac{1}{m_i}\sigma_{par}K_{ej}f(>v_{esc})\sum_{m_j} F_j E_I(m_j) \left[\frac{(2^{2-q_{ej}}-1)m_i^{2-q_{ej}}}{m_l^{2-q_{ej}} - m_s^{2-q_{ej}}}\right], \tag{13}$$

where K_{ej} is the proportionality constant between total ejected mass and the kinetic energy of the impact, $f(>v_{esc})$ is the fraction of ejecta escaping the parent body per impact, F_j is the differential flux of impactors of mass m_j (including gravitational focusing by Saturn at the G Ring), E_I is the kinetic energy of the impactor, and q_{ej} is the assumed differential index for the ejecta mass distribution. The quantity in brackets is the fraction of the total ejected mass that is in the mass range described by mass bin m_i and state bin n_i for an ejecta distribution with m_l and m_s as the masses of the largest and smallest ejected particles. The size distribution of the ejecta produced by each impact is determined by q_{ej} and the total mass ejected, $M_{ej} = K_{ej}E_I$.

For K_{ej} and $f(>v_{esc})$, we use the parameterizations of Greenberg *et al.* (1978) for impacts into unbonded quartz sand (UQS) and weakly bonded quartz sand (BQS). For UQS, $K_{ej} \approx 2 \times 10^{-8}$, and for BQS, $K_{ej} \approx 1.5 \times 10^{-9}$. The fraction of ejecta escaping is $f(> v_{esc}) \approx c_{ej}v_{esc}^{-9/4}$, with $c_{ej} \sim 10^4$ for UQS and $c_{ej} \sim 10^6$ for BQS. The escape velocity of parent bodies in the G Ring is reduced due to the tidal

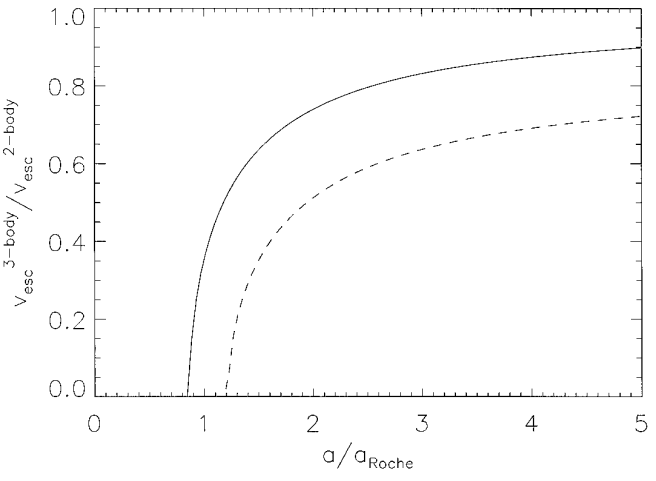

FIG. 2. Ratio of the angle-averaged three-body escape velocity (from Canup and Esposito (1995)) to the standard two-body escape velocity as a function of $a/a_{\rm Roche}$, where $a_{\rm Roche}$ is the Roche radius. The three-body escape velocity (which accounts for tidal effects of the central planet) is a function of the mass ratio of the two intereacting bodies; the solid line is for a mass ratio of 10^{-6}, whereas the dashed line is for a mass ratio of 0.1. The G Ring is located at $a \sim 1.3a_{\rm Roche}$.

force of Saturn. Figure 2 is a plot of the ratio of the angle-averaged three-body escape velocity to the standard two-body escape velocity as a function of $a/a_{\rm Roche}$. The curves in Fig. 2 are just two "slices" through the surface plot in Fig. 4b from Canup and Esposito (1995) for two different mass ratios of colliding bodies. At the G Ring, located at about $1.3a_{\rm Roche}$ for ice densities, the three-body angle-averaged escape velocity for a particle from a much larger parent body is about $\sim 0.5(2GM_{\rm par}/R_{\rm par})^{1/2}$, or about 75 cm/sec for a 2-km-radius parent. The Greenberg *et al.* (1978) parameterizations yield $f(>v_{\rm esc}) \sim 0.6$ for UQS and $f(>v_{\rm esc}) = 1$ for BQS, where $v_{\rm esc}$ is the two-body escape velocity of the impacted body. Given the uncertainty in the value of $c_{\rm ej}$, we let $f(>v_{\rm esc}) = 1$ and assume that all meteoroid impact ejecta escape their parent body.

While each meteoroid impact produces new ring particles, it also depletes the amount of regolith on the parent body. Assuming that the particles in a parent body's regolith are uniformly mixed, the rate of change in the number of mass m_i particles in the regoliths of parent bodies due to meteroid impact can be approximated as

$$\left.\frac{d(N_i - n_i)}{dt}\right|_{\rm ej} \approx -\frac{[\sigma_{\rm par} K_{\rm ej} f(>v_{\rm esc}) \Sigma_{m_j} F_j E_{\rm I}]}{M_{\rm reg}} (N_i - n_i), \tag{14}$$

where the quantity in brackets is just the total ejected mass per second, $M_{\rm reg}$ is the total regolith mass, and $(N_i - n_i)$ is the total number of mass m_i particles contained in the regolith of parent bodies at a given time. Particles lost from the regolith are reprocessed into the size distribution for impact ejecta as described above.

Grain Removal due to Drag

There are several destructive and removal processes outlined in SC93 that act on G Ring particles, including grain destruction by ion sputtering and meteoroid impact and grain removal due to plasma or Poynting–Robertson drag. SC93 identify plasma drag as the dominant process for the dust, with a 1-μm radius particle crossing the width of the ring in $t_{\rm drag}(1\ \mu{\rm m}) \sim 8$–800 years. The rate of removal or free particles due to a drag process is approximately

$$\left.\frac{dn_i}{dt}\right|_{\rm drag} \approx -n_i \frac{1}{t_{\rm drag}(1\ \mu{\rm m})} \left(\frac{1\ \mu{\rm m}}{r}\right), \tag{15}$$

where $t_{1\ \mu{\rm m}}$ is just the removal time for a 1-μm-radius particle. Since the rate of removal due to drag forces is inversely proportional to particle radius, the effect of drag is to make the size distribution shallower, decreasing the power-law index by 1.

Catastrophic Fragmentation of Ring Particles

For larger particles, destruction by catastrophic meteoroid impacts is significant. The dividing line between impacts that erode a body, i.e., eject a small amount of mass relative to the total target mass and leave the target intact, and impacts that catastrophically destroy a body, i.e., fragment an entire target into pieces much smaller than the original target, occurs at an impactor energy of about (Grün *et al.* 1984)

$$E_{\rm I} = 10^7\, m_{\rm par}, \tag{16}$$

where $m_{\rm par}$ is the mass of the target ring particle in grams and $E_{\rm I}$ is the impactor kinetic energy in ergs. For impact velocities typical of external impactors at the G ring (25 km/sec), particles of mass $m_{\rm par}$ are catastrophically destroyed by impactors with $m_{\rm imp} \geq 3 \times 10^{-6}\, m_{\rm par}$. The rate of removal of free particles due to catastrophic disruption is then just

$$\left.\frac{dn_i}{dt}\right|_{{\rm cat},r} \approx -n(i)\pi r_i^2 \sum_{m_j > 3\times 10^{-6} m_i} F_j. \tag{17}$$

Since the rate of removal due to catastrophic destruction is proportional to the radius of the grains squared, this process can steepen the size distribution of material in size regimes where the impacting flux of meteoroids capable of destroying the particles does not decrease more rapidly with size than $1/r^2$ (Colwell 1996). This is the case for

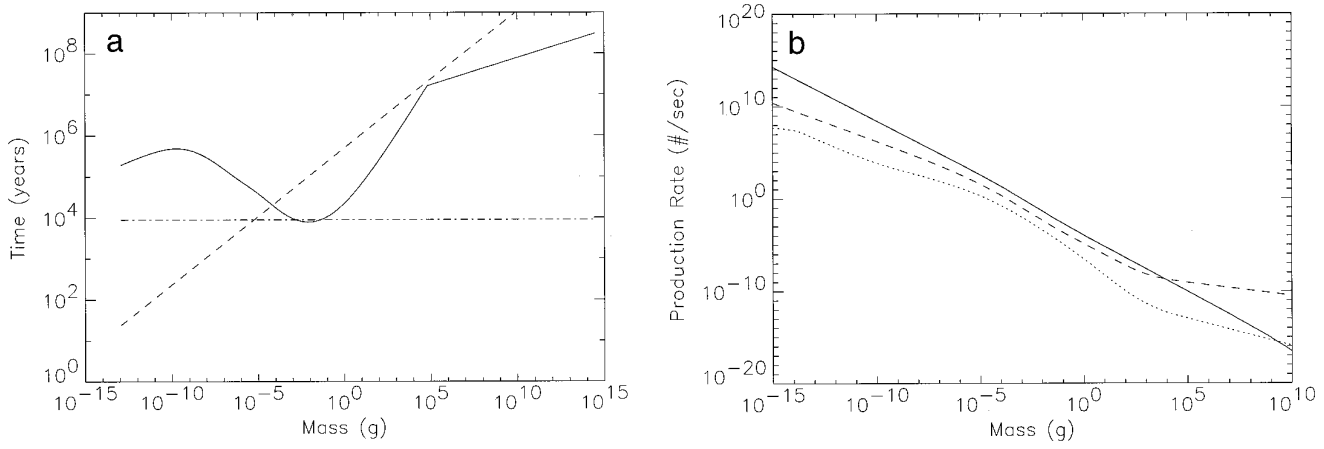

FIG. 3. (a) Destruction or removal time for a G Ring particle is plotted as a function of ring particle mass. The solid line is the lifetime against catastrophic disruption by external impact (using the high-flux impactor model), the dashed line is the time for a particle to orbitally evolve due to plasma drag through a distance equal to the width of the G Ring [assuming $t_{\rm drag}$ (1 μm) = 80 years], and the dot–dashed line is the collision time for a ring particle with a parent body (for a total parent body cross section of 40 km^2). (b) Production rate of a G Ring particle is plotted as a function of ring particle mass. The solid line is the production rate due to meteoroid impact of parent bodies (using the high-flux model, $q_{\rm ej}$ = 4.5, and a total parent body cross section of 40 km^2), the dashed line is the particle production rate due to collisional release during parent body collisions, and the dotted line is the production rate due to catastrophic disruption of free ring particles (again using the high-flux impactor model).

impactors with masses between about 10^{-15} and 3×10^{-8} g (where the impacting flux is relatively flat) and ring particles with masses between about 5×10^{-10} and 0.01 g. Figure 3a is a plot of the removal times as a function of particle mass due to the three processes considered in this model: removal due to accretion onto a parent body (dot–dashed line, assuming $\sigma_{\rm par}$ = 40 km^2), destruction by catastrophic meteoroid impact (solid line, assuming high-flux model), and removal due to plasma drag [dashed line, assuming $t_{\rm drag}$ (1 μm) = 80 years]. Drag dominates the removal of particles with masses up to about 10^{-5} g, impact destruction is significant for masses between about 10^{-7} and 10 g, and accretion onto the parent bodies dominates for all larger bodies.

The catastrophic fragmentation of ring particles may also lead to the production of smaller free debris. Few data are available that are relevant to the regime of high-velocity collisions between very low mass particles. The catastrophic disruption of a dust particle might yield both vaporization and solid debris fragments, the latter of which might or might not be well described by the power-law distributions typical of collisions between larger bodies. With these limitations in mind, we parameterize the debris produced by catastrophic impacts in the following manner. First, we assume that no solid debris is produced if the impact energy exceeds the energy required to vaporize the ring particle, or if $E_{\rm I} > m_{\rm par} L_{\rm v}$ where $L_{\rm v}$ is the latent heat of vaporization of water. By this simple criterion, an impactor with a velocity of 25 km/sec would vaporize ring particles of mass $m_{\rm par}$ when $m_{\rm imp} \geq 0.01\ m_{\rm par}$. For lower-energy impacts which still exceed the catastrophic fragmentation threshold, we assume that the largest fragment has a mass fraction of $f_{\rm l}$ = 0.1 [shown by Davis and Ryan (1990) to be typical of the highest-energy collisions] and that the debris distribution has a slope given by Eq. (8). The rate of production of free particles due to catastrophic disruption of larger particles is then just

$$\left.\frac{dn_i}{dt}\right|_{\rm cat,p} = \sum_{m_k > m_i/0.1} \left.\frac{dn_k}{dt}\right|_{\rm cat,r} \left(\frac{F(>3\times10^{-6}\,m_{\rm k}) - F(>0.01\,m_{\rm k})}{F(>3\times10^{-6}\,m_{\rm k})}\right) m_k \left[\frac{(2^{2-q_{\rm ej}}-1)m_i^{2-q_{\rm ej}}}{m_{\rm l}^{2-q_{\rm ej}} - m_{\rm s}^{2-q_{\rm ej}}}\right], \quad (18)$$

where $\sum_{m_k > m_i/0.1} dn_k/dt_{\rm cat,r}$ is the total rate of catastrophic disruptions [from Eq. (17)] of all particles massive enough to produce a fragment of mass m_i, the quantity in parentheses is the fraction of these catastrophic disruptions that do not result in complete vaporization, and m_k is the total mass produced by each fragmenting event. The bracketed quantity is the fraction of the total fragmented mass that is in the mass range described by mass bin m_i for an ejecta distribution with $m_{\rm l}$ and $m_{\rm s}$ as the masses of the largest and smallest ejected particles and a slope of $q_{\rm ej}$. We assume $m_{\rm s}$ is the smallest mass followed in our simulations and we ignore the mass contribution of the impactor since it is negligible for nonvaporizing impacts.

Figure 3b is a plot of the production rate of particles as

a function of particle mass due to the impact ejection from meteoroid bombardment of the parent bodies (solid line, using the high-flux model, $q_{ej} = 4.5$ and $\sigma_{par} = 40$ km^2), collisional release during collisions between parent bodies (dashed line, determined by σ_{par} and the size distribution of particles contained in the parent body regoliths), and production from the catastrophic fragmentation of free ring particles as described above (dotted line, a function of the free particle size distribution). Impact ejection from bombardment of the parent bodies dominates the production of ring particles.

We also investigated an additional ring particle removal process: ring particle diminution due to erosive micrometeoroid impacts with impact energies lower than the limit in Eq. (17). Simulations with particles moving to smaller bins as they were eroded at a rate analogous to that in Eq. (17) (but in this case integrating only over the impacting flux with m_{imp} less than $3 \times 10^{-6}\ m_i$) were indistinguishable from those without free particle erosion for our typical run times (up to 100,000 years). This is because most of the impacting mass is in impactors smaller than about 100 μm in radius, and these micrometeoroids are erosive (as opposed to destructive) only to ring particles larger than about 1 g in mass. The erosive lifetime of a 1-g particle is about 24,000 years (see SC93), much longer than the recollision time with a parent body. Since the rate of change of the size of a particle due to erosion is independent of particle size (dr/dt = constant, see, e.g., SC93), erosion does not change the slope of the size distribution, but over long times it will shift the whole size distribution to smaller sizes and reduce the total amount of material (e.g., Colwell 1996). The total amount of material produced during erosive impacts of ring particles is typically at least an order of magnitude smaller than that produced by erosive impacts of parent bodies.

Thus, the time evolution of the number of free particles, n_i, and the total number of particles (free and in regolith), N_i, is just

$$n_i(t_1) = n_i(t_0) + \Delta t \left(\left.\frac{dn_i}{dt}\right|_{acc} + \left.\frac{dn_i}{dt}\right|_{rel} + \left.\frac{dn_i}{dt}\right|_{ej} + \left.\frac{dn_i}{dt}\right|_{cat,r} + \left.\frac{dn_i}{dt}\right|_{cat,p} + \left.\frac{dn_i}{dt}\right|_{drag} \right) \quad (19)$$

and

$$N_i(t_1) = N_i(t_0) + \Delta t \left(\left.\frac{dn_i}{dt}\right|_{ej} + \left.\frac{d(N_i - n_i)}{dt}\right|_{ej} + \left.\frac{dn_i}{dt}\right|_{cat,r} + \left.\frac{dn_i}{dt}\right|_{cat,p} + \left.\frac{dn_i}{dt}\right|_{drag} \right). \quad (20)$$

V. RESULTS

For each of our simulations, we begin with the initial debris distribution formed by the disruption of a hypothetical G Ring progenitor satellite and evolve this distribution forward in time as described in the previous section. Figures 4 and 5 show the evolution of the mass distribution of free G Ring material for different initial distributions and choices for the slope of ejecta produced by meteoroid bombardment, q_{ej}. For these results we used our baseline set of parameters: ejecta scaling parameters appropriate for unbonded quartz sand, t_{drag} (1 μm) = 80 years, Δa = 1000 km, $\sigma_{par} = 40$ km^2, and the high-impactor-flux model. In each figure the initial distribution is shown with a dashed line. The energy of the impactor that disrupted the G Ring progenitor (which determines f_l and the slope of the initial debris distribution) and the assumed slope of ejecta produced by meteoroid impact were input parameters.

The character of the mass distribution of free material for the final states in all of the runs can be described by five regimes. First are the parent bodies, which form a small bump visible at the high mass end of the distribution. At masses somewhat smaller than the parent bodies is a regime of macroscopic particles whose number is determined by a balance between reaccretion onto the parent bodies and collisional release during parent body collisions and whose slope is just the slope of the initial distribution. At some smaller size (which varies from 10^{-6} to 10^3 g as a function of q_{ej} and the slope of the initial debris distribution), production of particles due to ejection by meteoroid impacts into the parent bodies begins to contribute significantly to the number of free particles and the slope of the distribution changes from that of the initial distribution to q_{ej}. At particle masses of about 10^{-2} g, the size distribution steepens slightly due to the effect of catastrophic fragmentation of grains by meteoroid impact (e.g., in Fig. 4a the steady-state distribution has a slope of $q \sim 5.1$ from 10^{-4} to 0.1 g). At sizes smaller than about 10^{-7} g (determined by the choice of t_{drag}), the distribution reflects a balance between removal due to drag and production by meteoroid bombardment. This balance gives a power-law distribution with a slope that is simply the assumed slope of meteoroid-produced ejecta (q_{ej}) flattened by one [to ($q_{ej} - 1$)] due to the radius-dependent drag removal (e.g., Burns *et al.* 1984).

Figure 4a shows the evolution of the mass distribution for a barely catastrophic disruption of the progenitor satellite, with $f_l = 0.5$ and an initial debris distribution with a size differential index of $q = 1.8$. The size at which meteoroid ejection yields numbers of free particles in excess of the initial distribution is a function of the choice of q_{ej}; Figs. 4a and b show respectively $q_{ej} = 4.5$ and 5.0. Figure 5 is for an initial disruption event close to the estimated median value of f_l, with $f_l = 0.1$ and $q = 2.9$, with a $q_{ej} = 5.0$.

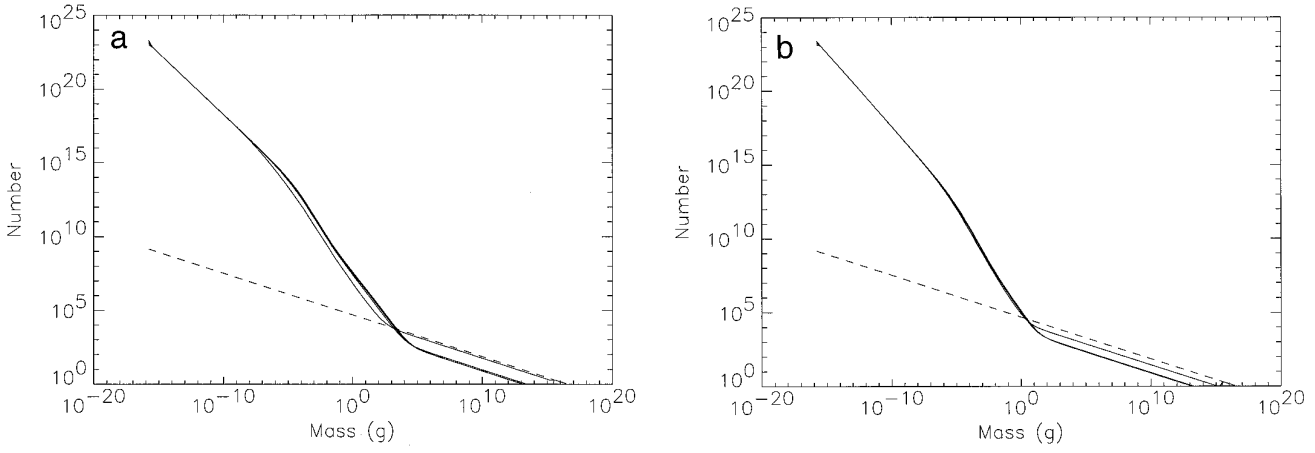

FIG. 4. Size distribution of free G Ring particles as a function of particle mass is shown for various times (UQS, 40 km^2, high flux). The initial distributions are shown by a dashed line and assumed a $f_l = 0.5$ and $\sigma_{par} = 40$ km^2. (a) $q_{ej} = 4.5$; distributions are shown at 7000, 12000, 35,000, and 72,000 years. The parent bodies constitute the small peak between $\sim 5 \times 10^{15}$ to 5×10^{16} g. (b) $q_{ej} = 5.0$; distributions are shown at 9700, 38,000, 71,000 years. Here the parent bodies fall between $\sim 3 \times 10^{15}$ and 4×10^{16} g.

Macroscopic G Ring Particle Population

The simulations shown in Figs. 4 and 5 were each run with a set of baseline parameters chosen to maximize the predicted population of millimeter-sized particles in the G Ring (maximum cross section of parent bodies, high impactor flux, narrow ring width, UQS target surface). Table I lists the free parameters and results from each run, as well as the predicted surface number density of macroscopic particles with $r > 0.13$ mm from each of our final distributions. Simulations with $\delta = 1$ (where δ is the fraction of regolith ejected when two parent bodies collide) yield macroscopic populations similar to those in Table I for cases that are consistent with the photometric and PWS/PRA observations. Macroscopic number surface densities are also relatively insensitive to the exact choice for the mass range of the initial G Ring parent bodies, for a given choice of σ_{par}. Although these calculations are all for the densest portion of the G Ring, the σ_n values implied by our model are orders of magnitude smaller than those derived purely from the worst-case-photometric upper limits of the surrounding "empty" regions!

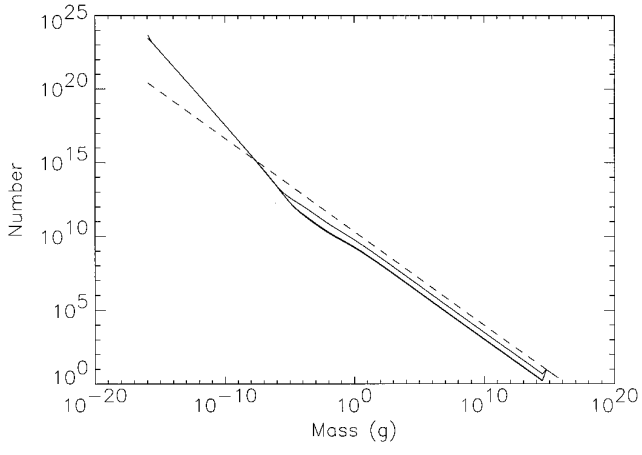

FIG. 5. Size distribution of G Ring particles as a function of mass shown at 12,000, 37,000, and 60,000 years (UQS, 40 km^2). Here the initial (dashed) distribution describes a more catastrophic initial progenitor disruption, with $f_l = 0.1$. $q_{ej} = 5.0$ was assumed.

Extrapolations to Apparently Empty Regions near the G Ring

The Cassini spacecraft will likely avoid the G Ring itself, instead passing through the gaps surrounding the ring. The size distributions computed here can be appropriately scaled for those "empty" regions, assuming that similar processes would be required to maintain a population of small particles in the regions surrounding the G Ring as in the ring itself. That is, particles would arise from collisions between and meteoroid bombardment of macroscopic parent bodies created in some earlier satellite disruption. The upper limit on charged particle lifetime in the gaps surrounding the G Ring implies a maximum surface area of macroscopic bodies about one-tenth that of the G Ring. A σ_{par} value of 4 km^2 yields small-particle optical depths an order of magnitude smaller than those in Table I. Thus, the σ_n values in Table I should be divided by 10 to give an upper limit on macroscopic surface number densities in the gaps surrounding the G Ring.

Comparison of Model Predictions to G Ring Photometry and Voyager PWS/PRA Data

While our G Ring model contains multiple free parameters, we have found that many can be constrained by photo-

TABLE I
Simulation Results of G Ring Evolution and Associated Macroscopic Particle Population

Radius of progenitor (km)	f_l; N_{par}	q_{ej}	Steady-state total optical depth	Predicted m_{rms} for Voyager PWS/PRA impact detections (g)	Surface number density (#/m^2) of macroscopic particles $\sigma_n(r > 0.13$ mm)
3	0.5; 5	3.5	1.0×10^{-6}	1.4×10^{-6}*	0.62
		4.5	4.0×10^{-6}	1.6×10^{-7}	0.132
		5.0	4.0×10^{-6}	2.2×10^{-8}	0.0032
2.6	0.1; 20	3.5	1.1×10^{-6}	9.6×10^{-7}*	1.04
		4.5	4.0×10^{-6}	1.1×10^{-7}	0.072
		5.0	4.4×10^{-6}	1.5×10^{-8}	0.0026
2.1	0.08; 22	3.5	1.1×10^{-6}	1.0×10^{-6}*	1.03
		4.5	4.0×10^{-6}	1.1×10^{-7}	0.084
		5.0	3.8×10^{-6}	9.2×10^{-8}	0.017

Note. All runs used a total parent body cross section of 40 km^2, the high-impactor-flux model, t_{drag} (1 μm) = 80 years, and UQS target surfaces. The energy of the initial disruption that forms the ring determines the mass fraction of the largest fragment, f_l. N_{par} is the number of parent bodies and q_{ej} is the assumed size power-law index for ejecta produced by meteoroid erosion. The predicted m_{rms} values should be compared with the $1.8 \times 10^{-8\pm1}$-g value derived from the V2 PWS/PRA impact detections; values inconsistent with this are marked with an asterisk. Spacecraft like Voyager and Cassini are vulnerable to impacts by particles with $r > 0.13$ mm or $m > 10^{-5}$ g. The $\sigma_n(r > 0.13$ mm) values listed here may be divided by 10 to correspond to the gaps surrounding the G Ring.

metric or PWS/PRA data. From SC93, we know both the observed small particle optical depth ($\tau_G \sim 1$–2×10^{-6}) and an upper limit on the optical depth of macroscopic particles ($\tau_{big} \sim 6 \times 10^{-7}$). Both the total and macroscopic optical depths were computed for each of our runs and compared with these data. As an additional constraint, we also computed the rms mass which would have been detected by impacts to the PWS/PRA Voyager instruments as they passed through a ring with our theoretical distribution of material. To do this we calculated impact probabilities of the Voyager spacecraft from Eq. (5) (using an effective spacecraft cross-sectional area of 1.66 m^2 from Gurnett *et al.* 1983) for impacts with all particles with masses above the PWS/PRA impact detection mass threshold of $\sim 5.4 \times 10^{-9}$ g. We then drew random numbers to determine which impacts occurred, calculated the corresponding $\langle m^2 \rangle^{1/2}$ value, and compared this prediction with the Voyager dust impact estimate of $m_{rms} = 1.8 \times 10^{-8\pm1}$.

In Table II we list the model parameters and their effect on the total optical depth and m_{rms}. The total optical depth is roughly proportional to the total cross section of the parent bodies divided by the ring width. Initial distributions with $f_l < 0.08$ yield steady-state distributions with overly high m_{rms} values and macroscopic optical depths that exceed the photometric upper limit. Values of $f_l > 0.5$ are plausible and result in macroscopic particle populations even smaller than those listed in Table I. Experimental results have found a range of q_{ej} values, with $q_{ej} > 3$ appropriate for the majority of ejecta generated by hypervelocity impacts (e.g., Asada 1985). We find that $q_{ej} \leq 3.5$ produces mass distributions with m_{rms} values significantly larger than those detected by the PWS/PRA impact analysis, while $q_{ej} \geq 6.0$ yields distributions so steep than the PWS/PRA instruments would have been unlikely to experience any impacts with particles above the detection mass threshold. Values of q_{ej} between 4.5 and 5.0 yield the best agreement. Drag removal times with t_{drag} (1 μm) > 20 years produced distributions with sufficient optical depth. The low model impactor flux produced enough total optical depth only when combined with a t_{drag} (1 μm) = 800 years.

Discussion

Our model assumes that all parent bodies remain on collisional orbits. Parent bodies could occupy stable noncolliding configurations if they are locked in horseshoe orbits or if their orbital spacing is greater than 3.5–10R_{Hill}, where R_{Hill} is the Hill radius (see Chambers *et al.* 1996, Gladman 1993). Since at the G ring, $r/R_{Hill} \sim 0.5$, twenty-two 2-km-radius parent bodies could all be spaced with $\Delta a = 10R_{Hill}$ in a region only 880 km in width. It is therefore plausible that the parent bodies are noncolliding and that $dn_i/dt|_{rel} = 0.0$. An example of a run without parent body collisions is shown in Fig. 6; the final distribution has a total optical depth of 3.6×10^{-6}, an $m_{rms} = 1.6 \times 10^{-7}$ g, and a macroscopic surface number density of $\sigma_n = 0.091$. Simulations without parent body collisions typically yield optical depths and m_{rms} values similar to those of the runs with parent body collisions (since the population of the smallest particles is dominated by production due to exter-

nal meteoroid impacts into the parent bodies) and associated macroscopic surface number densities that are up to an order of magnitude smaller than those in Table I.

We have considered a particle density of 1 g/cm^3; densities less than about 1.3 g/cm^3 and coefficients of restitution less than $\varepsilon \lesssim 0.6$ yield results similar to those in Tables I and II for a given value of σ_{par}. For higher densities, there is no significant tidal restriction on accretion and our hypothesized colliding regolith-covered bodies would be expected to reaccrete into a single body. This appears inconsistent with the proton absorption signatures (Hood 1989); however, higher densities cannot be ruled out, since the orbits of the parent bodies could have become collisionally isolated from one another.

We describe the size distribution of ejecta produced from a meteoroid impact as a single power law with a variable differential size index q_{ej}. A value of q_{ej} between about 4 and 5 is then required to match both the total ring optical depth and the PRA/PWS results. This, combined with removal due to plasma drag, yields a steady-state size distribution with $q \sim 3$–4 for the smallest ring particles.

TABLE II
G Ring Model Parameters

Range of Parameters			Variation in output	
Parameter	Baseline	Range	m_{rms}	τ
Progenitor radius	3.0 km	3.0 km	1.6×10^{-7}	4.0×10^{-6}
		1.5 km	1.5×10^{-7}	9.8×10^{-7}
f_l	0.5	0.5	1.6×10^{-7}	4.0×10^{-6}
		0.06	1.2×10^{-6}	4.4×10^{-6}
σ_{par}	40 km^2	40 km^2	1.6×10^{-7}	4.0×10^{-6}
		10 km^2	1.5×10^{-7}	9.8×10^{-7}
Δa	1000 km	1000 km	1.6×10^{-7}	4.0×10^{-6}
		5000 km	1.5×10^{-7}	8.0×10^{-7}
q_{ej}	4.5	3.5	1.4×10^{-6}	1.0×10^{-6}
		5.0	2.2×10^{-8}	3.8×10^{-6}
t_{drag} (1 μm)	80 years	8 years	1.4×10^{-7}	4.0×10^{-7}
		800 years	1.5×10^{-7}	2.8×10^{-6}
Meteoroid flux	High	High	1.6×10^{-7}	4.0×10^{-6}
		Low	1.6×10^{-8}	2.0×10^{-7}
Target	UQS	UQS	1.6×10^{-7}	4.0×10^{-6}
		BQS	2.4×10^{-8}	3.2×10^{-7}

Note. τ is the total optical depth. m_{rms} is the predicted rms mass that would be detected by the Voyager PWS/PRA antennas. σ_{par} is the cross-sectional area of parent bodies. f_l is the mass fraction of the largest fragment remaining after the initial disruption of the progenitor satellite. q_{ej} is the differential size index of ejecta produced by meteoroid bombardment.

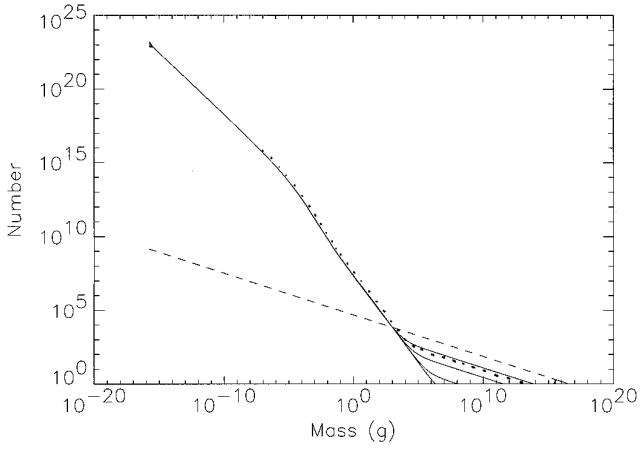

FIG. 6. Same simulation parameters as in Fig. 4a (f_l = 0.5, q_{ej} = 4.5), but here the parent bodies are assumed to occupy noncolliding orbits. Size distributions of free particles are shown at t = 0, 9500, 24,000, 52,000, and 60,000 years. The dotted line is the steady-state distribution from Fig. 4a for comparison.

SC93 compared phase curves produced by various power-law distributions with G Ring observations at four viewing geometries and found best agreement for a size index of $q = 6$.

It is possible that some physical process (or processes) not included in our model causes a steepening of the size distribution of submicrometer-sized particles. For instance, high-velocity impacts into icy grains likely produce some vaporization, and recondensation may yield particles at a preferred size in the submicrometer size range. Canup *et al.* (1993) found that the combined effects of planetary oblateness and radiation pressure can steepen the distribution of dust ejecta over a limited size range through size-dependent eccentricity perturbations which affect recollision rates with the source bodies. At the G Ring, however, this effect would cause size distribution steepening in only the 100-μm to centimeter size range for kilometer-sized parent bodies [Canup *et al.* 1993, their Eq. (13)]—sizes too large to affect photometric results. It is also possible that the steepness of the G Ring dust size distribution was overestimated by SC93; a slope of $q \sim 6$–7 is difficult to reconcile with recent color measurements by Nicholson *et al.* (1996) (see Throop and Esposito 1996). Additional observational constraints on the size distribution of G Ring material may be forthcoming with further analysis of the 1995 ring plane crossing data.

VI. CONCLUSIONS

The agreement of our evolutionary model with photometric and Voyager PRA/PWS results supports the idea that the G Ring was formed by the disruption of a progenitor satellite, and that its population of short-lived particles

is continuously maintained by a belt of parent bodies. These parent bodies are likely the largest remaining fragments from the original disruption event, and their similar sizes prevent them from mutually reaccreting due to tidal forces (see papers by Colwell and Esposito 1992, 1993, and Canup and Esposito 1995). We find best agreement with photometric, charged particle absorption and PWS/PRA impact data for (1) a progenitor satellite 1.5–3 km in radius; (2) a disruption event with $f_l \geq 0.08$ or with $Q \leq 3.7Q^*$, where Q is the specific impact energy and Q^* is the specific impact energy at the catastrophic fragmentation threshold; (3) drag removal time scales for 1-μm particles > 20 years; and (4) meteoroid impact ejecta size distributions with a differential power-law index of $q_{ej} \sim 4$–5.

Our predicted number surface densities of macroscopic particles in and around the G Ring are orders of magnitude lower than those determined from observational upper limits. While the Cassini spacecraft is an ideal detector of such particles (which are hazardous to various spacecraft subsystems), it is extremely unlikely that the spacecraft will encounter any during its passages through the ring plane near the G Ring. Our macroscopic surface number density estimates imply probabilities for a safe (i.e., collisionless) passage of Cassini through the middle of the G Ring during a single ring plane crossing with a spacecraft inclination of 45° that are greater than 92.7% in all cases, and greater than 99.1% for runs that concur with Voyager 2 PWS/PRA m_{rms} estimates. The probability of a single safe passage through ''empty'' regions neighboring the G Ring is estimated to be greater than 99.3% for all cases.

ACKNOWLEDGMENTS

We thank the members of the CU ''Ring Group''—Glen Stewart, Mihaly Horanyi, Josh Colwell, and Henry Throop—for their contributions to this work, as well as Jeff Cuzzi for his comments on an earlier version of our model. We benefited from helpful reviews from Mark Showalter and Dick Durisen. This work was supported by the Cassini Project.

REFERENCES

Asada, N. 1985. Fine fragments in high-velocity impact experiments. *J. Geophys. Res.* **90,** 12445–12453.

Burns, J. A., M. R. Showalter, and G. E. Morfill. 1984. The ethereal rings of Jupiter and Saturn. In *Planetary Rings* (R. Greenberg and A. Brahic, Eds.), pp. 200–274. Univ. of Arizona Press, Tucson.

Burns, J. A., M. R. Showalter, J. N. Cuzzi, and J. B. Pollack 1980. Physical processes in Jupiter's ring: Clues to its origin by Jove! *Icarus* **44,** 339–360.

Canup, R. M., and L. W. Esposito 1995. Accretion in the Roche zone: Co-existence of rings and ringmoons. *Icarus* **113,** 331–352.

Canup, R. M., and L. W. Esposito 1996. Formation of the Moon from an impact-generated disk. *Icarus* **119,** 427–446.

Canup, R. M., J. E. Colwell, and M. Horanyi 1993. Size distributions of satellite dust ejecta: Effects of radiation pressure and planetary oblateness. *Icarus* **105,** 363–369.

Chambers, J. E., G. E. Wetherill, and A. P. Boss 1996. The stability of multi-planet systems. *Icarus* **119,** 261–268.

Colwell, J. E. 1994. The disruption of planetary satellites and the creation of planetary rings. *Planet. Space Sci* **42,** 1139–1149.

Colwell, J. E. 1996. Size distributions of circumplanetary dust. *Adv. Space Res.* **17**(12), 161–170.

Colwell, J. E., and L. W. Esposito 1990. A numerical model of the uranian dust rings. *Icarus* **86,** 530–560.

Colwell, J. E., and L. W. Esposito 1992. Origins of the rings of Uranus and Neptune: I. Statistics of satellite disruptions. *J. Geophys. Res.* **97,** 10,227–10,241.

Colwell, J. E., and L. W. Esposito 1993. Origins of the rings of Uranus and Neptune: II. Initial conditions and ring moon populations. *J. Geophys. Res.* **98,** 7387–7401.

Cuzzi, J. N., and R. H. Durisen 1990. Bombardment of planetary rings by meteoroids: General formulation and effects of Oort Cloud projectiles. *Icarus* **84,** 467–501.

Cuzzi, J. N., *et al.* 1989. *Abundance and Size Distribution of Ring Material Outside of the Main Rings of Saturn.* Unpublished report of Cassini 1/20/89 workshop.

Davis, D. R., and E. V. Ryan 1990. On collisional disruption: Experimental results and scaling laws. *Icarus* **83,** 156–182.

Divine, N. 1989. *Risk Analysis for Saturn Ring Particles Impacting the Cassini Orbiter.* JPL IOM 5217-89-153.

Esposito, L. W., and J. E. Colwell 1989. Creation of the Uranus rings and dust bands. *Nature* **339,** 605–607.

Gladman, B. 1993. Dynamics of systems of two close planets. *Icarus* **106,** 247–263.

Greenberg, R., J. F. Wacker, W. K. Hartmann, and C. R. Chapman 1978. Planetesimals to planets: Numerical simulation of collisional evolution. *Icarus* **35,** 1–26.

Grün, E., G. E. Morfill, and D. A. Mendis 1984. Dust–magnetosphere interactions. In *Planetary Rings* (R. Greenberg and A. Brahic, Eds.), pp. 275–332. Univ. of Arizona Press, Tucson.

Grün, E., H. A. Zook, H. Fechtig, and R. H. Giese 1985. Collisional balance of the meteoritic complex. *Icarus* **62,** 244–272.

Gurnett, D. A., E. Grün, D. Gallagher, W. S. Kurth, and F. L. Scarf 1983. Micron-sized particles detected near Saturn by the Voyager plasma wave instrument. *Icarus* **53,** 236–254.

Hood, L. L. 1989. Investigation of the Saturn dust environment from the analysis of energetic charged particle measurements. In *Cassini AO,* Vol. XIII.

Housen, K. R., and K. A. Holsapple 1990. On the fragmentation of asteroids and planetary satellites. *Icarus* **84,** 226–253.

Housen, K. R., R. M. Schmidt, and K. A. Holsapple 1983. Crater ejecta scaling laws: Fundamental forms based on dimensional analysis. *J. Geophys. Res.* **88,** 2485–2499.

Housen, K. R., L. L. Wilkening, C. R. Chapman, and R. Greenberg 1979. Asteroidal regoliths. *Icarus* **39,** 317–351.

Nicholson, P. D., M. R. Showalter, L. Dones, R. G. French, S. M. Larson, J. J. Lissauer, C. A. Mcghee, P. Seitzer, B. Sicardy, and G. E. Danielson 1996. Observations of Saturn's ring-plane crossings in August and November 1995. *Science* **272,** 509–515.

Showalter, M. R., and J. N. Cuzzi 1993. Seeing ghosts: Photometry of Saturn's G Ring. *Icarus* **103,** 124–143.

Smith, B. A., and 28 Colleagues 1982. A new look at the Saturn system: The Voyager 2 images. *Science* **215,** 505–537.

TAN, G., AND G. TSUYUKI 1989. *Update to IOM 313-3-316-GHT: Saturn's Rights Hazards Assessment: Spacecraft Vulnerability to Critical Particle Masses.* JPL IOM 313/3-015-GHT.

THROOP, H. B., AND L. W. ESPOSITO 1996. Constraints on particle sizes in Saturn's G Ring from ring plane crossing observations. *Bull. Am. Astron. Soc.* **XVIII,** 1125.

TSINTIKIDIS, D., D. BURNETT, L. J. GRANROTH, S. C. ALLENDORF, AND W. S. KURTH 1994. A revised analysis of micron-sized particles detected near Saturn by the Voyager 2 plasma wave instrument. *J. Geophys. Res.* **99,** 2261–2270.

VAN ALLEN, J. A. 1983. Absorption of energetic protons by Saturn's ring G. *J. Geophys. Res.* **88,** 6911–6918.

WEIDENSCHILLING, S. J., C. R. CHAPMAN, D. R. DAVIS, AND R. GREENBERG 1984. Ring particles: Collisional interactions and physical nature. In *Planetary Rings* (R. Greenberg and A. Brahic, Eds.), pp. 367–415. Univ. of Arizona Press, Tucson.